1-1-2020

Evaluation of microstructure variation of TC11 alloy after electroshocking treatment

Lechun Xie

Chang Liu

Yanli Song

Haojie Guo

Zhongqi Wang

See next page for additional authors

Authors

Lechun Xie, Chang Liu, Yanli Song, Haojie Guo, Zhongqi Wang, Lin Hua, Liqiang Wang, and Lai-Chang Zhang

Original Article

Evaluation of microstructure variation of TC11 alloy after electroshocking treatment

Lechun Xie [a,b,1], Chang Liu [a,b,1], Yanli Song [a,b], Haojie Guo [a,b], Zhongqi Wang [a,b], Lin Hua [a,b,], Liqiang Wang [c], Lai-Chang Zhang [d]*

[a] *Hubei Key Laboratory of Advanced Technology for Automotive Components, Wuhan University of Technology, Wuhan 430070, PR China*
[b] *Hubei Collaborative Innovation Center for Automotive Components Technology, Wuhan University of Technology, Wuhan 430070, PR China*
[c] *State Key Laboratory of Metal Matrix Composites, School of Materials Science and Engineering, Shanghai Jiao Tong University, No. 800 Dongchuan Road, Shanghai 200240, PR China*
[d] *School of Engineering, Edith Cowan University, 270 Joondalup Drive, Joondalup, Perth, WA 6027, Australia*

ARTICLE INFO

ABSTRACT

Electro-shocking treatment (EST) has been investigated as a pathway to optimise the microstructure and mechanical properties of titanium alloys. The thermal conditions introduced by EST resulted in a phase transformation from α to β. The fraction of β phase decreased from 25.27% to 19.47% after EST for 0.02 s, which was possibly caused by the recrystallization of α phase. The application of EST for 0.04 s resulted in an increase in volume fraction of the β phase to 26.95%. The energy introduced by EST resulted in changes to the direction and intensity of texture within the microstructure with the texture intensity of the α phase increasing from 4.94 to 8.52, and that of β both increased from 3.35 to 9.88 after 0.04 s EST.

1. Introduction

Titanium alloys exhibit excellent properties such as low density, high strength-to-weight ratio, high melting temperature, high corrosion resistance, high strength, and high heat resistance [1–6]. TC11 (Ti-6.5Al-3.5Mo-1.5Zr-0.3Si) alloy is an $\alpha + \beta$ titanium alloy (TC11 in China and BT9 in Russia) [7] and is mainly used in compressor discs, blades, drums, and other parts of aircraft engines, as well as aircraft structural parts [8]. The mechanical properties of TC11 are crucial for their aerospace and industrial applications [9]. The α and β phase fractions of TC11 affect its mechanical properties. Therefore, it is imperative to investigate the phase transformation thermodynamics and kinetics of TC11 under different conditions.

Various efforts have been made to improve the comprehensive properties of TC11 using different heat treatment methods. Huang et al. [10,11] reported that the tensile strength

---

and elongation of TC11 can be improved by hot compressing, and hot tensile tests can increase the grain size and volume fraction of the β phase. It has been reported that the microstructure of TC11 changes after heat treatment [12,13]. Song et al. [14] found that TC11 shows α phase globularization upon deformation at 920–980 °C over the strain rate range of 0.01–10 s^{-1}. Jing et al. [15] reported that when exposed to the deformation temperatures of 1000 and 1050 °C at the strain rate of 10 s^{-1} TC11 shows the α → β phase transformation. Li et al. [16] showed that the sliding of the α and β grain boundaries is the major mechanism for the super-plasticity deformation of TC11 at 940–990 °C over the strain rate range of 0.001–0.01 s^{-1}. These methods utilized for varying the microstructure and improving the mechanical properties of TC11 alloy are based on heat treatments. However, since heat treatment affects the entire sample, it is difficult to control the partial microstructure of alloys using heat-treatment methods. Moreover, heat treatment is a time-consuming and energy-consuming process and requires harsh conditions such as high temperature, high pressure, and vacuum. Therefore, it is imperative to develop a simple, energy-efficient, and rapid phase transformation method for controlling the partial microstructure of titanium alloys.

Electropulse treatment can improve the comprehensive properties of a material by applying high-density pulse current in a short time. Electropulse treatment can repair the local microcracks of titanium alloys and promotes their healing by coupling the thermal and non-thermal effects of pulse current [17–19]. This treatment can also improve the uniform elongation and plasticity of titanium alloys [20,21]. It can also relax the surface residual stress and improve the fatigue life of titanium alloys [22,23]. In addition, electropulse treatment can optimize the defects and reduce the concentration of the residual stress in titanium alloys. Electroshocking treatment (EST) is similar to electropulse treatment. However, the electro current energy and current density of EST are much higher than those of electropulse treatment, and the pulse current is more stable. EST is suitable for the treatment of bulk materials and large components. It can be used for treating materials with the sizes ranging from the micro-scale to the macro-scale. The EST energy can be adjusted by changing the pulse current and treatment time, which can control the influence region further. Therefore, EST can be used to optimize the microstructure of TC11 alloy.

In this study, TC11 alloy was subjected to EST for various durations. The temperature variation during the EST was monitored using an infrared thermal imager. Scanning electron microscopy (SEM) and X-ray diffraction (XRD) were used to analyze the microstructure and phase transformation of TC11. The texture of the alloy was analyzed using the electron backscatter diffraction (EBSD) technique.

Table 1 – EST durations of the specimens.

Specimen number	EST time (s)
No. 0	0
No. 2	0.02
No. 3	0.03
No. 4	0.04

2. Experimental procedure

2.1. Specimen preparation and EST treatment

TC11 alloy was provided by Baoji Titanium Industry Co., Ltd. (China). Small cylindrical specimens with a diameter of 5 mm and a length of 10 mm were machined from the raw rod material by wire-electrode cutting. After machining, the surface oxide layer was removed using abrasive papers. The EST of the specimens was carried out for different durations. The EST current used was 4200 A. The EST durations of the specimens are listed in Table 1.

The temperature variations of the specimens were monitored using an infrared thermal imager (Fotric-220) with a response wavelength of 8–14 μm. The temperatures were calibrated using FotricAnalyzIR software, and the temperature vs. time curves of the specimens were obtained and analyzed. The distance between the infrared thermal imager and the specimen was 20 cm, and the measurement temperature was 20 °C. The EST equipment and temperature monitor used in this study are shown in Fig. 1(a).

2.2. Microstructure characterization

The microstructures of the specimens were examined using SEM (Fig. 1(b)). The specimens were cut along the central axis of the cylinder and were prepared using the standard metallographic method. The specimens were ground using different abrasive papers (240 + 600 + 1200 + 4000 grit). The specimens were then polished using a solution containing OPS (a suspension of SiO$_2$) and 40% H$_2$O$_2$. After polishing, the specimens were cleaned ultrasonically in ethanol for 10 min. The XRD analysis of the specimens was carried out on a PANalytical
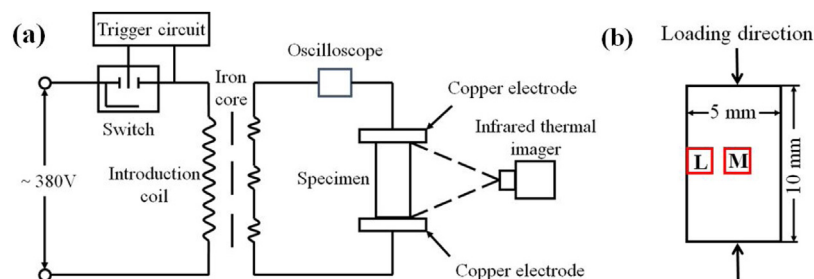

Fig. 1 – (a) EST equipment and temperature monitor; (b) Positions of microstructure characterization: the left (L) and middle (M) areas.
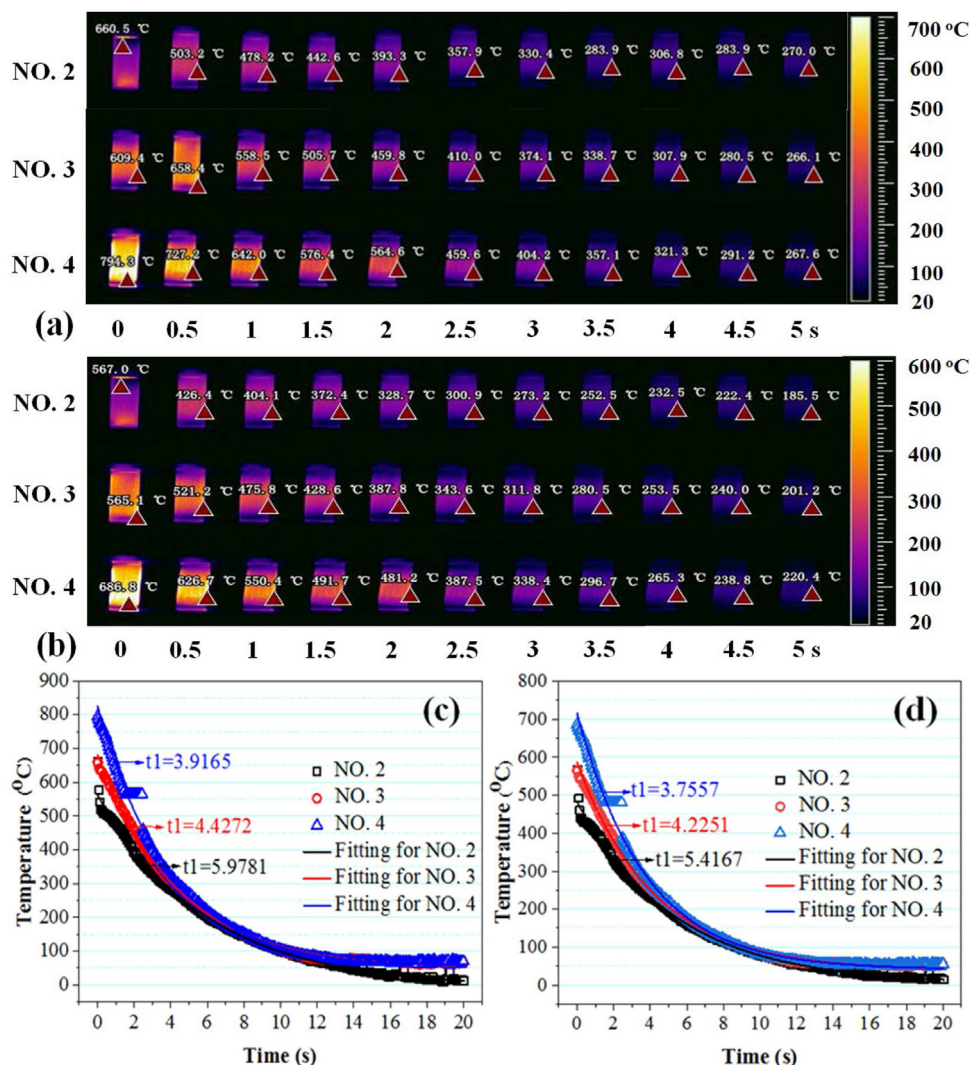
Fig. 2 – Temperature variation and photographs of the specimens under different emissivities ((a) 0.15 and (b) 0.23), and the temperature vs. time curves of the specimens under different emissivities ((c) 0.15 and (d) 0.23).

Empyrean diffractometer with Cu-Kα radiation (λ = 1.54056 Å) in the reflection mode. The XRD measurements were carried out over the 2θ range of 30–90° at the scanning speed of 3°/min. SEM (Zeiss, Germany) was used to analyze the phase structure variations of the specimens at 10 kV. In order to analyze the variation in the phase contents of the specimens, their SEM images were processed using ImageJ software. The phase area of the specimens was equivalent to their phase content.

2.3. EBSD analysis

The grain orientation and texture in the middle areas of the specimens were investigated using EBSD. An EBSD detector equipped with HKL Technology CHANNEL 5 software on Zeiss Ultra Plus X-Max 50 was utilized for the data acquisition, orientation mapping, and texture analysis. The pole figures and inverse pole figures of the α and β phases were obtained. The scanning area of the specimens before and after the EST was 100 μm × 50 μm. All the data were processed and analyzed

by CHANNEL 5, and the grain orientation and texture of the specimens were analyzed.

3. Results and discussion

3.1. Temperature variation during the EST

The photographs and temperature variation of the specimens at different emissivities during the EST are shown in Fig. 2. Different wavelengths monitored during the temperature measurement correspond to different emissivities. Since the range of the infrared wavelength monitored using the infrared temperature imager was 8–14 μm, the emissivity range was selected to be 0.15–0.23 during the temperature calibration [24]. Fig. 2(a) shows the temperature variation of the specimens under the emissivity of 0.15. The temperature decreased from 660.5 to 270 °C over a period of 5 s. With an increase in the EST duration, the initial temperature of the specimens increased. The specimen treated for 0.04 s showed

the highest max temperature (794.3 °C), while that treated for 0.02 s showed the lowest max temperature. As the input energy increased with an increase in the EST duration, the thermal effect became more significant with an increase in the EST duration. Fig. 2(b) shows the temperature of the specimens under the emissivity of 0.23. These specimens showed temperatures lower than those subjected to the emissivity of 0.15. The temperature variation trend shown in Fig. 2(b) was consistent with that shown in Fig. 2(a). The increase in the emissivity resulted in a decrease in the energy received by the infrared thermal imager. The temperature vs. time curves of the specimens are shown in Fig. 2(c) and (d). These curves show the variation of the highest temperature of the specimens with time during the EST. The symbols denote the data recorded by the infrared thermal imager and the solid lines correspond to the curves fitted with the mathematical function ExpDec1: $y = A_1{}^*exp(-x/t_1) + y0$. It can be observed that with an increase in the EST duration from 0 to 8 s, the temperature of the specimens decreased rapidly. The specimen treated for 0.04 s showed the highest cooling rate.

Based on the relevant physical parameters of the TC11 alloy, the temperature variation ΔT can of the specimens could be calculated theoretically. The temperature rise ΔT was calculated using Eq. (1).

$$\Delta T = \frac{\int_0^{t_p} \rho j^2(t)dt}{c_p d} \tag{1}$$

where ρ is the resistivity, $j(t)$ is the current density during the EST, d is the density, t_p is the EST time, and C_p is the specific heat capacity of the material. For the TC11 alloy, the physical parameters were: ρ = 1.75 $\mu\Omega$ m, d = 4.48 g/cm^3, and C_p = 544.43 J/(kg K). The room temperature T_0 during the experiment was 20 °C. For the specimen treated for 0.04 s, t_p = 0.04 s, ΔT = 789.8 K. Hence, its maximum temperature ($T = \Delta T + T_0$) was calculated to be 809.8 °C. The calculated maximum temperatures for specimens 2 and 3 were 394.45 and 605.52 °C, respectively. The temperatures monitored using the infrared thermal imager and those calculated theoretically are shown in Fig. 3. The open and solid symbols denote the highest temperature obtained by the infrared thermal imager under the emissivities of 0.15 and 0.23, respectively. The solid star symbols represent the average values of the calculated results. The calculated values were consistent with the temperatures monitored using the infrared thermal imager.

During EST, a large amount of heat is generated in a very short time, and the corresponding thermal expansion appears in the interior of the specimen, generating potential thermal stress. The thermal stress of a specimen can be calculated using Eq. (2).

$$\sigma_{max} = E \cdot \alpha \cdot \Delta T_{max} \tag{2}$$

where α is the thermal expansion coefficient, E is the Young's Modulus, and ΔT_{max} is the max temperature increment. It can be observed from Eq. (2) that the thermal stress is proportional to the highest temperature increment. The thermal stresses of specimens 2, 3, and 4 were calculated to be 390.76, 611.02, and 824.19 MPa, respectively. The specimen treated for 0.04 s
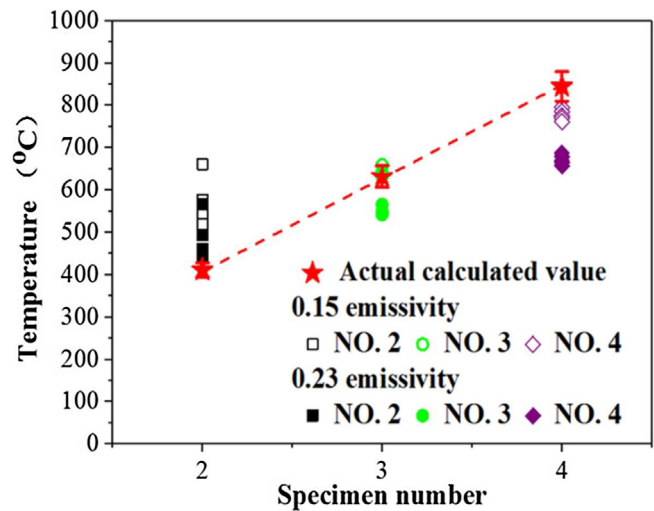

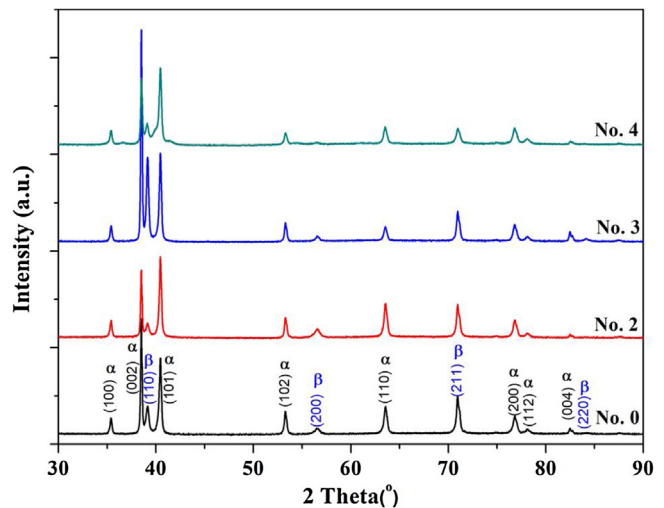**Fig. 3 – Temperatures calculated theoretically and monitored using the infrared thermal imager.**

Fig. 4 – XRD patterns of the specimens treated for various durations.

showed the highest thermal stress. The thermal stress caused microstructural variations in the specimens.

3.2. Microstructure characterization and analysis

The XRD patterns of the specimens treated for various durations are shown in Fig. 4. The specimens showed the diffraction peaks corresponding to the α-Ti (*hcp*) and β-Ti (*bcc*) phases. No additional phase was generated after the EST. The peak positions of the α and β phases did not change after the EST. However, the intensities of the α (002), α (101), and β (110) peaks changed, indicating that the grain orientation of the specimens depended on the EST parameters.

The morphologies of the left (L in Fig. 1(b)) and middle areas (M in Fig. 1(b)) of the specimens were examined by SEM. The low (×1,000)- and high (×5,000)-magnification SEM images of the specimens are shown in Figs. 5 and 6, respectively. It
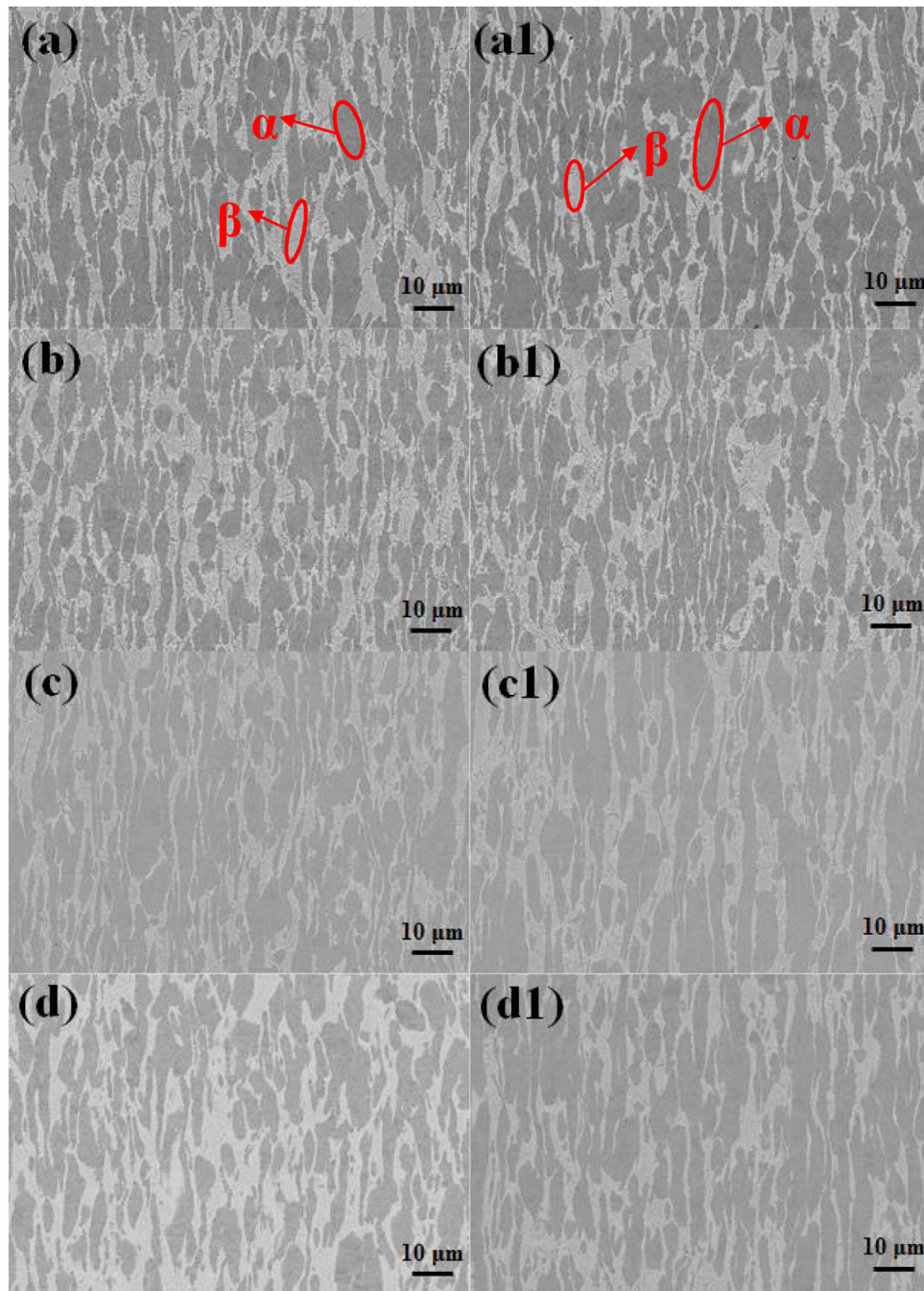
Fig. 5 – SEM images of the specimens before and after the EST: (a), (b), (c), and (d) show the morphologies of the middle area; (a1), (b1), (c1), and (d1) show the morphologies of the left area.

can be observed from Fig. 5(a) and (a1) that prior to the EST, the specimens consisted of the α (gray) and β (white) phases. These phases were distributed along the axial direction of the raw rod-shaped material because of the extrusion of the raw material. During the process of extrusion, the α and β phases deformed along the extrusion direction (the axial direction). When the EST was carried out for 0.02 and 0.03 s, the variation in the microstructure of the specimens was not significant (Fig. 5 (b), (b1), (c), and (c1)). However, when the EST was carried out for 0.04 s, the area of the white region (β phase) increased

(Fig. 5(d) and (d1)). The energy concentration during the EST increased the temperature of the specimen significantly. The temperature reached the α → β phase transformation temperature when the EST was carried out for 0.04 s. Hence, specimen 4 showed the α → β phase transformation.

Fig. 6 shows the high-magnification SEM images of the phases of the specimens treated for various durations. As can be observed from Fig. 6(a) and (a1), in the case of the untreated specimen, the secondary α phase precipitated from the β phase. The secondary α phase was different from the
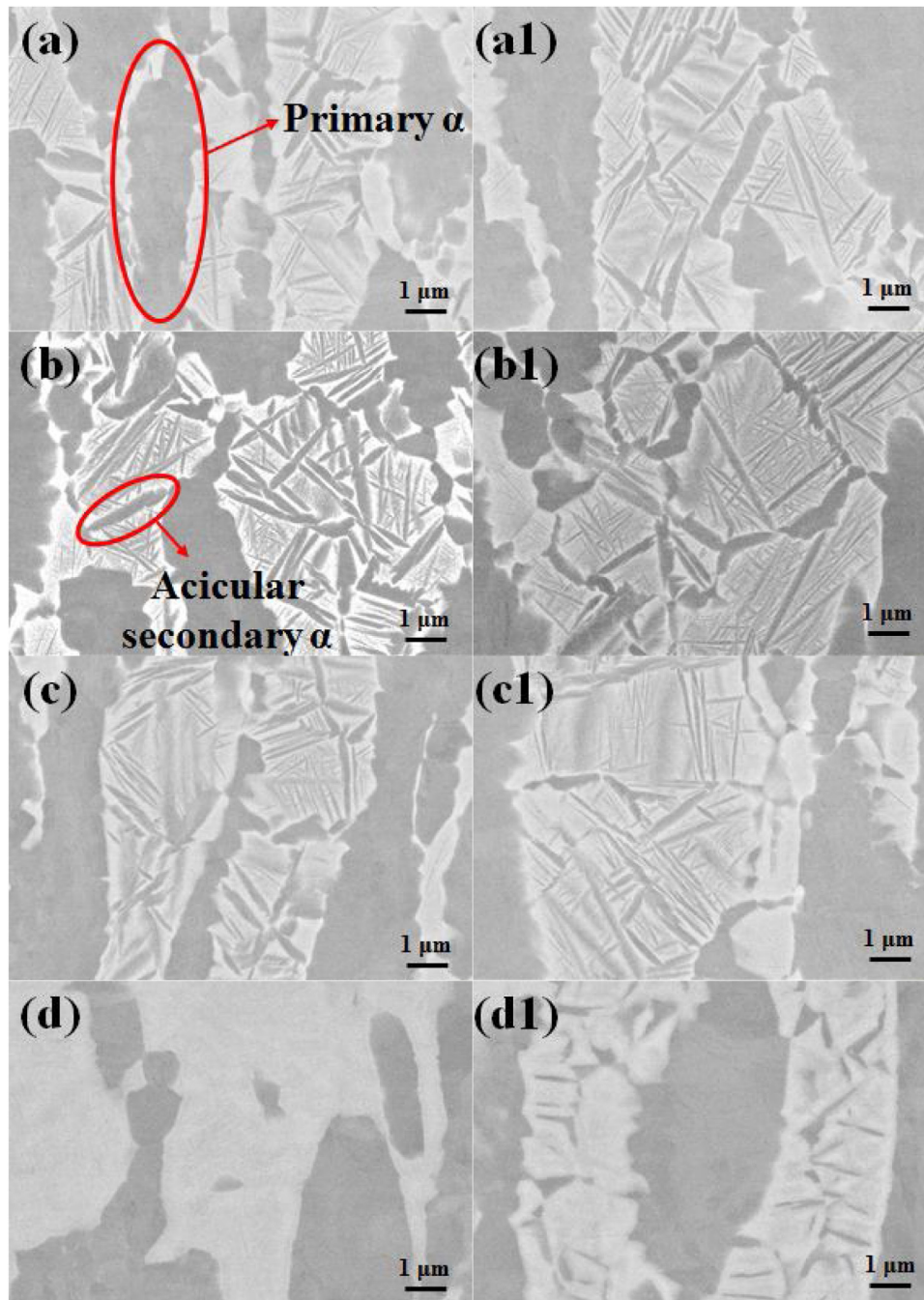
Fig. 6 – High-magnification SEM images of specimens 0, 2, 3, and 4: (a), (b), (c), and (d) show the morphologies of the middle areas of the specimens; (a1), (b1), (c1), and (d1) show the morphologies of the left areas of the specimens.

primary α phase. The primary α phase showed a round and columnar shape (in Fig. 5), while the secondary α phase was distributed in the β phase with the acicular dispersion. The acicular secondary α phase existed in the raw material and precipitated during the process of hot extrusion. When the EST was carried out for 0.02 or 0.03 s, the acicular secondary α phase did not transform to the β phase significantly (Fig. 6(b), (b1), (c), and (c1)). This is because the energy of current was not enough to affect the acicular secondary α phase. These results are consistent with those shown in Fig. 5. However,

when the EST was carried out for 0.04 s, the acicular secondary α phase transformed into the β phase significantly and no acicular secondary α phase was observed (Fig. 6(d)). Most of the acicular secondary α phases converted into the β phase. The acicular secondary α phase showed the α → β transformation. However, the primary α phase did not undergo significant transformation. At the edge (on the left area) of the specimens (Fig. 6(d1)), the intermediate phase transformation process of the acicular secondary α phase could be observed, and only a part of the acicular secondary α phase showed the phase trans-
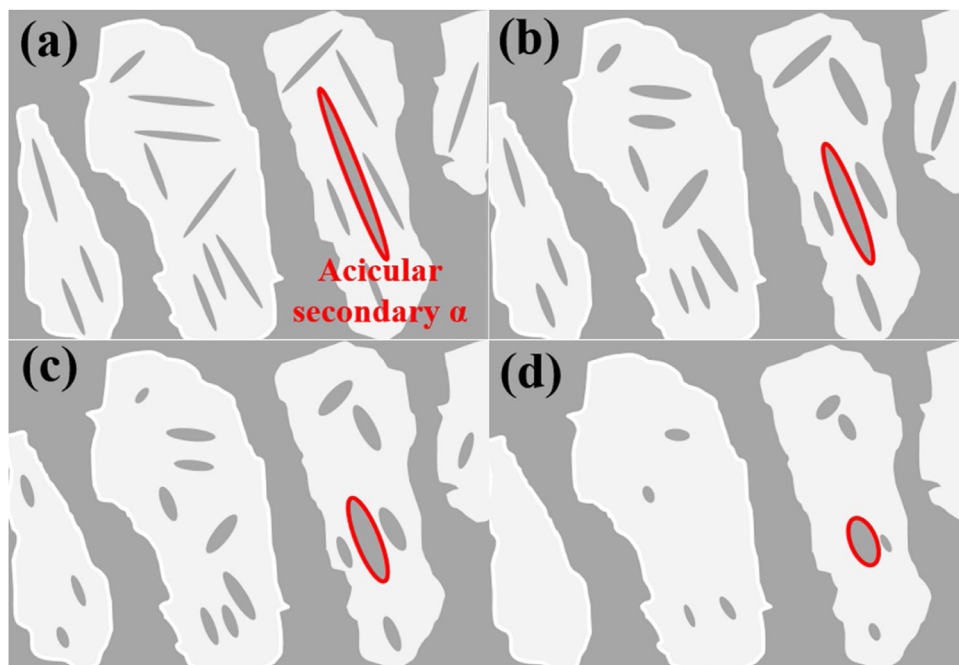
Fig. 7 – Variations in the acicular secondary α and β phases of the specimens treated for various durations: (a) untreated; (b) 0.02 s; (c) 0.03 s; (d) 0.04 s.

formation. The difference between the morphologies shown in Fig. 6(d) and (d1) can be attributed to the faster heat dissipation in the left area of the specimens than that in the middle area. The lower heat dissipation energy of the middle area accelerated the phase transformation process in this area and resulted in high energy concentration. From Fig. 6(d1), it can be observed that the tips of the acicular secondary α phase were blunt because of the melting of the tips. The potential principle is shown in Fig. 7.

Fig. 7 shows the variations in the acicular secondary α phase and β phase of the specimens caused by the thermal and non-thermal effects of the EST [25–29]. During the EST process, heat was generated at the tips of the secondary acicular α phase, which increased the temperature of the acicular α tips to the α → β phase transformation point instantaneously. The tips of the acicular α phase melted and cooled down, leading to the local phase transformation. The tips of the α phase transformed into the β phase, resulting in the formation of blunt tips. This demonstrates the thermal effect of the EST [27,30]. The "electron wind force" [26,27] and "current detour" [31–34] effects caused by the ultra-high current of the EST accelerated the atomic diffusion rate and promoted the local phase transition on the needle-like α tips, resulting in the globularlization of the α precipitate phase. The non-thermal effect can be attributed to the difference in the electrical resistivities of the α and β phases [35–37]. As a result, different currents passed through the α and β phases during the EST. The combination of the thermal and non-thermal effects promoted the transformation of the acicular secondary α phase to the β phase. Fig. 7 shows the evolution of the acicular secondary α phase after various EST durations. With an increase in the EST duration, the curvature radius of the acicular secondary α phase increased gradually. The secondary α phase showed

significant globularlization and its percentage decreased gradually.

3.3. Variation in the phase content

In order to accurately investigate the variation in the α and β phase contents of the specimens, their SEM images were obtained (Fig. 5) and were processed by ImageJ software. The corresponding processed images are shown in Fig. 8. The white regions denote the α phase, while the black ones denote the β phase. The β phase contents of the specimens could be determined by calculating the areas of the black portions in Fig. 8. The variation in the β phase contents at the two positions of the samples (based on the statistical calculation from 24 SEM images) is shown in Fig. 9.

Fig. 9 shows that the β phase content of the middle areas of the specimens first decreased and then increased. The average β phase content of the untreated specimen was 25.27%., which decreased to 19.47% when the EST was carried out for 0.02 s. After 0.04 s of the EST, the average β phase content increased to 26.95%. The quantitative analysis results were consistent with those obtained from Fig. 6. The β phase contents of the left and middle areas were similar. The variation trends of the β phase contents at the two positions were also similar. In the case of specimen 4 (before and after the EST), the average β phase content of the left area was lower than that of the middle area. This is consistent with the results obtained from Fig. 6(d) and (d1). This is because the acicular secondary α phase in the middle area almost completely transformed to the β phase. After the EST for 0.02 s, the average β phase content decreased because of the recrystallization of the α phase. The thermal measurement results shown in Fig. 3 revealed that the temperature of specimen 2 (∼660.5 °C) reached the
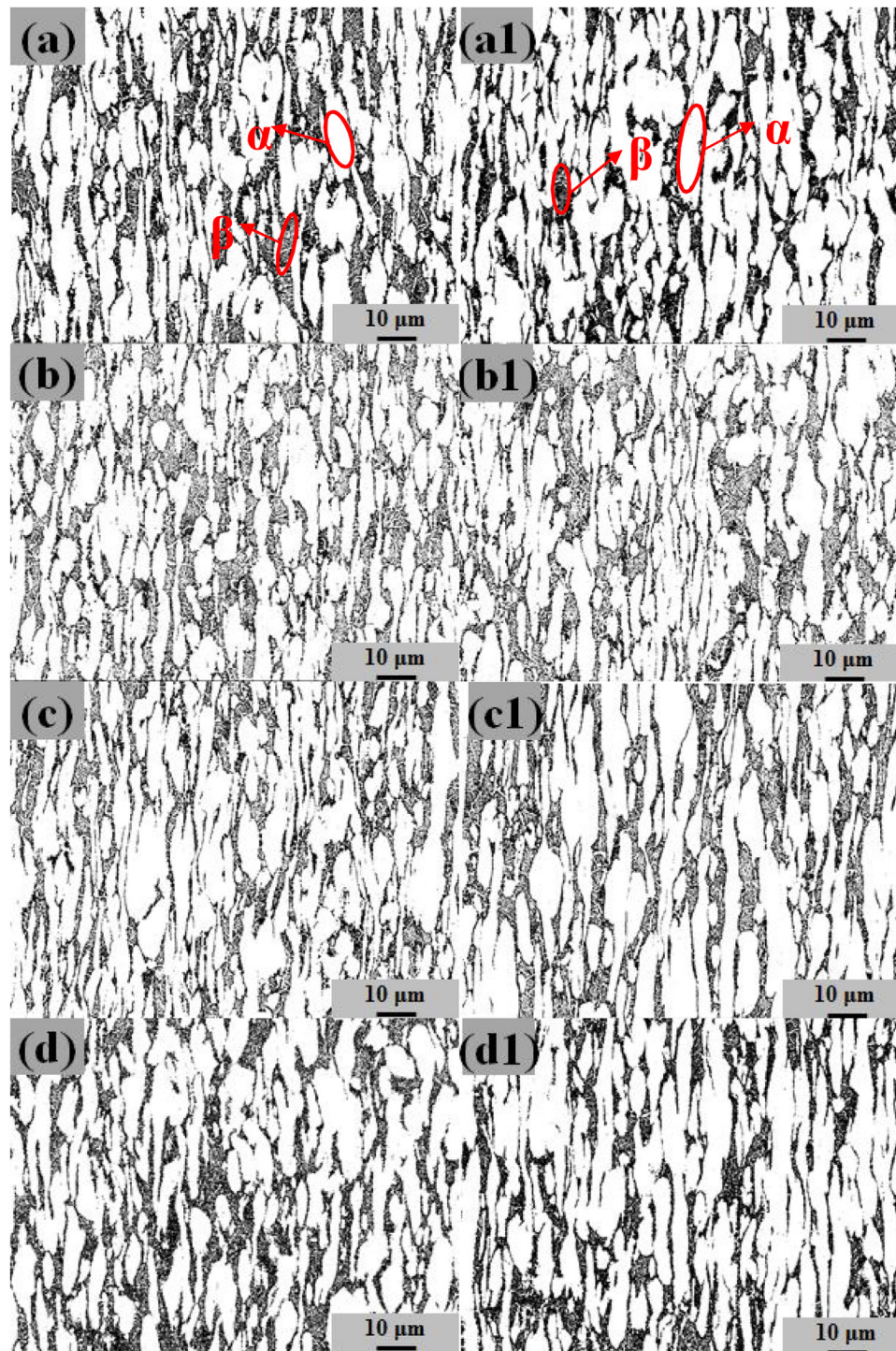
Fig. 8 – Processed SEM images of specimens 0, 2, 3, and 4: (a), (b), (c), and (d) show the morphologies of the middle area of specimens; (a1), (b1), (c1), and (d1) show the morphologies of the left area of the specimens.

recrystallization temperature of TC11 alloy (∼660 °C). The temperature at the middle of the specimen was higher than that at the surface (monitored by the infrared temperature imager), indicating the decrease in the β phase content. The results confirmed that EST changes the partial microstructure and phase content of TC11 alloy.

3.4. Grain orientation and texture analysis

Fig. 10 shows the grain orientation (β and primary α grains) (IPF Z) in the middle areas of the specimens before and after the EST. The grain orientation of the specimens changed significantly after the EST. After 0.04 s of the EST, some of the grains showed the tendency to grow mainly because of the
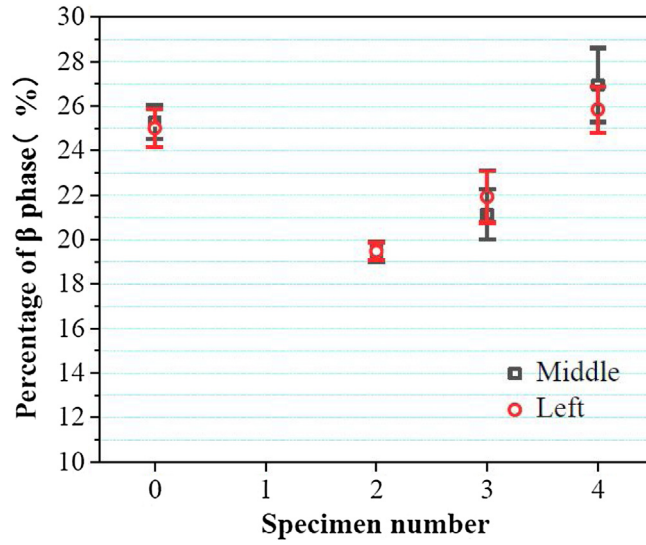
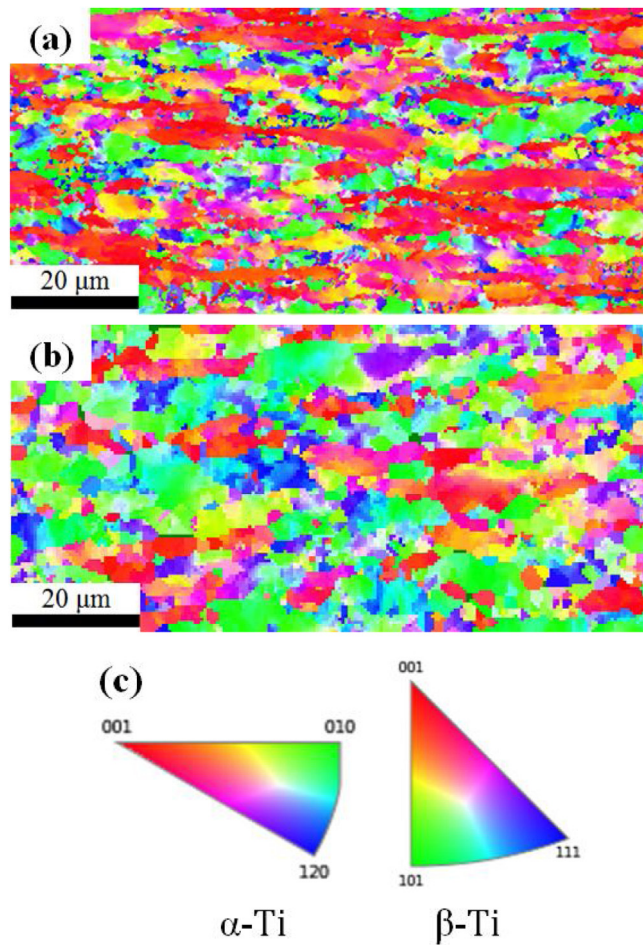Fig. 9 – β phase contents at two different locations of the specimens.

Fig. 10 – Grain orientation (IPF Z) in the middle areas of the specimens before and after the EST: (a) 0; (b) 4; (c) the standard orientation of α-Ti and β-Ti.
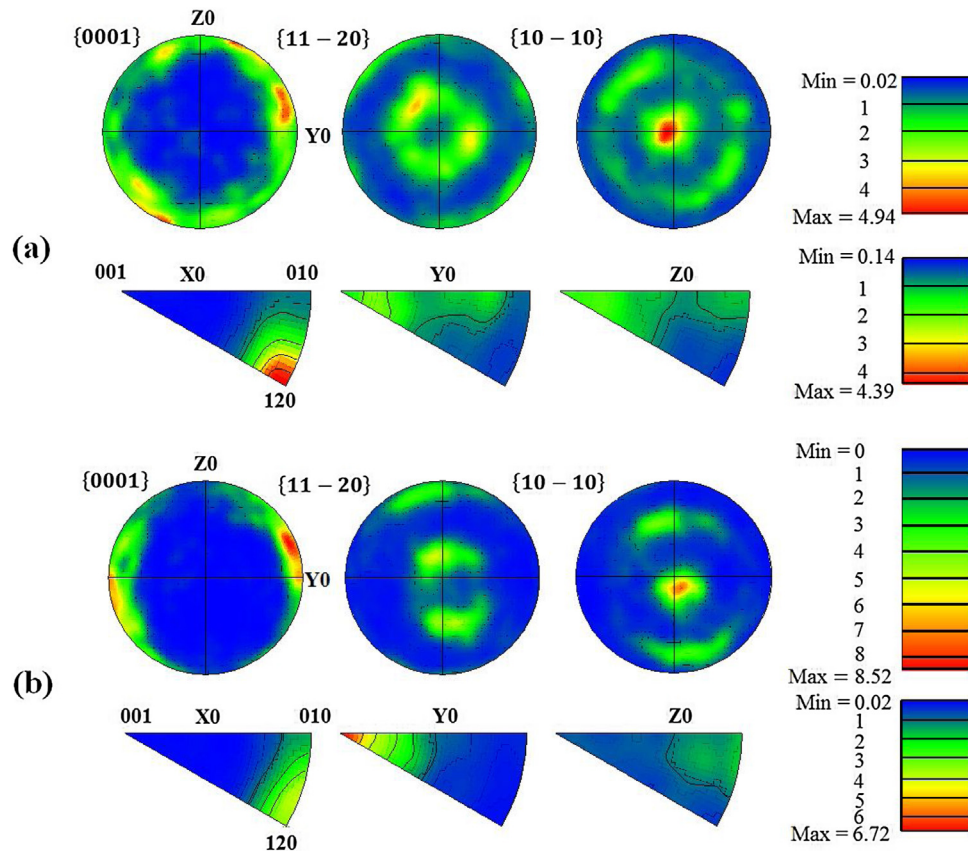
Fig. 11 – Pole and inverse pole figures of the α phase of the specimens before and after the EST: (a) 0; (b) 4.

acicular secondary α-to-β phase transformation. In order to investigate the texture distribution of the α and β phases of the specimens, their pole and inverse pole figures were obtained (Figs. 11 and 12).

Fig. 11 shows the texture distribution of the α phase of the specimens before and after the EST. It can be observed from Fig. 11(a) that the texture intensity of {10–10} < 120 > was the highest, I_{max} = 4.94, and the texture direction was parallel to the X_0 direction. After 0.04 s of the EST (in Fig. 11(b)), the texture intensity and direction changed significantly. The intensity of the texture parallel to the X_0 (120) direction decreased, while that of the texture parallel to the Y_0 (001) direction increased. The value of I_{max} was 8.52. This indicates that the phase transformation after the EST changed the α texture (including the intensity and direction) of the alloy.

Fig. 12 shows the texture distribution of the β phase of the specimens before and after the EST. It can be observed from Fig. 12(a) that in the case of the untreated specimen, the texture appeared in the (101) direction and was parallel to the Y_0 direction. Moreover, the maximum texture intensity, I_{max}, was 3.35. When the EST was carried out for 0.04 s (in Fig. 12(b)), the texture intensity of the (101) plane decreased. But the texture intensity of the (001) plane increased, and it was parallel to the X_0 direction. After 0.04 s of the EST, the texture changed to {100}<001> and the max intensity, I_{max}, was 9.88. It can be observed from Figs. 11 and 12, that the EST changed the texture direction of the α phase from the X_0 to the Y_0 direction and that of the β phase from the Y_0 to the X_0 direction.

This texture variation can be attributed to the phase transformation caused by the energy concentration occurring during the EST, which contributed to the improvement in the texture intensity of the alloy.

4. Conclusions

TC11 alloy was subjected to EST and the variations in its microstructure were investigated.

(1) After the EST, the phase morphology of the alloy changed significantly and its temperature reached the α → β transformation point. The acicular secondary α tips melted and cooled down in advance, resulting in the α → β phase transformation and the spheroidization of the acicular secondary α tips.

(2) The β phase content of the alloy first increased and then decreased with an increase in the EST duration. The average β phase content of the alloy decreased from 25.27% to 19.47% after 0.02 s of the EST. It then increased to 26.95% with a further increase in the EST duration to 0.04 s. The variation in the β phase content can be attributed to the recrystallization of the α phase and its transformation to the β phase.

(3) The texture intensity of the α phase increased from 4.94 to 8.52, while that of the β phase increased from 3.35 to 9.88 after the EST. The texture direction of the α phase
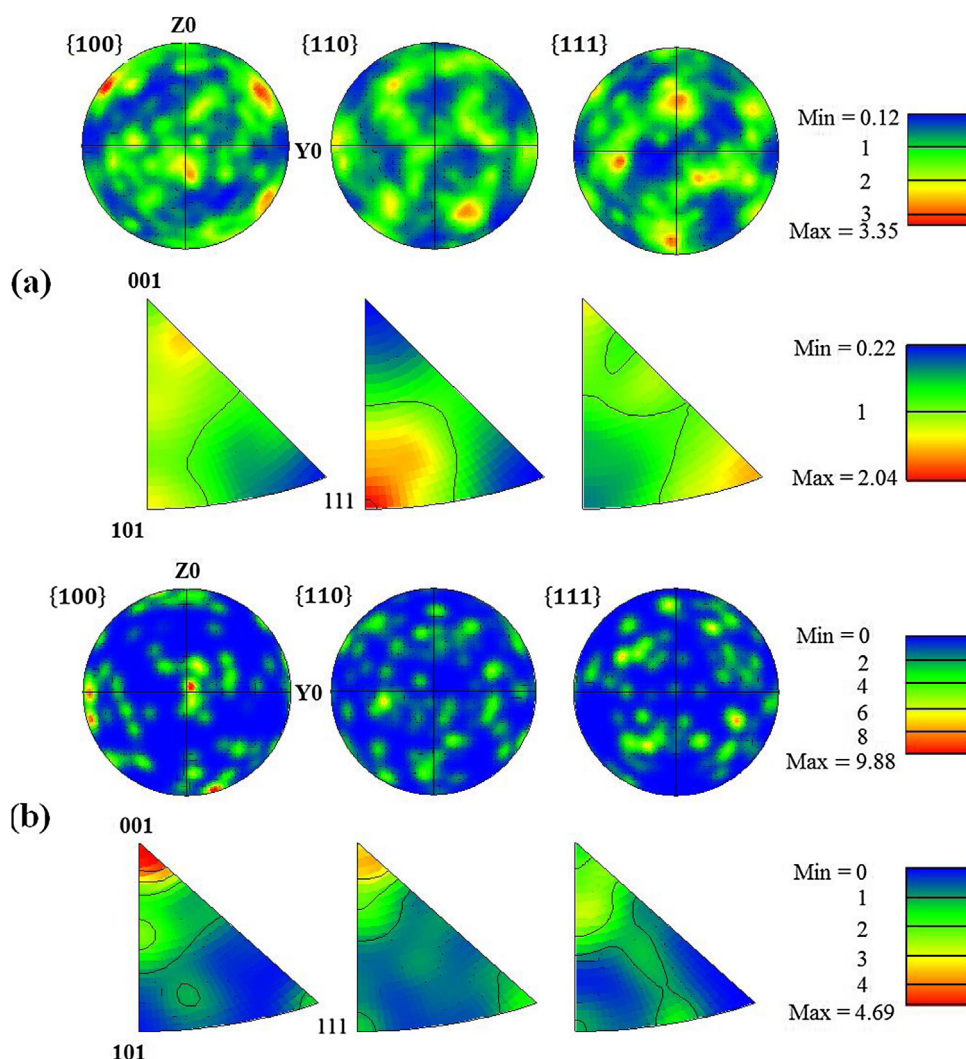
Fig. 12 – Pole and inverse pole figures of the β phase of the specimens before and after the EST: (a) 0; (b) 4.

changed from the X_0 to the Y_0 direction, while that of the β phase changed from the Y_0 to the X_0 direction. This can be attributed to the phase transformation caused by the concentration of energy during the EST.

The results showed that EST can modify the microstructure, phase content, and texture distribution of TC11. Hence, EST is a simple and efficient method to modify the microstructure of titanium alloys.

Data availability

The raw/processed data required to reproduce these findings cannot be shared at this time as the data also forms part of an ongoing study.

Conflict of interest statement

The authors declared that they have no conflict of interest to this work.

CRediT authorship contribution statement

Lechun Xie: Conceptualization, Data curation, Formal analysis, Investigation, Methodology, Writing - original draft. **Chang Liu:** Conceptualization, Data curation, Formal analysis, Investigation, Methodology, Writing - original draft. **Yanli Song:** Investigation, Methodology, Software, Validation, Visualization. **Haojie Guo:** Investigation, Methodology, Software, Validation, Visualization. **Zhongqi Wang:** Investigation, Methodology, Software, Validation, Visualization. **Lin Hua:** Conceptualization, Funding acquisition, Project administration, Supervision, Resources, Writing - original draft. **Liqiang Wang:** Writing - review & editing. **Lai-Chang Zhang:** Writing - review & editing.

Acknowledgements

REFERENCES

[1] Wang L, Xie L, Shen P, Fan Q, Wang W, Wang K, et al. Surface microstructure and mechanical properties of Ti-6Al-4V/Ag nanocomposite prepared by FSP. Mater Charact 2019;153:175–83.

[2] Hafeez N, Liu S, Lu E, Wang L, Liu R, Zhang L-C. Mechanical behavior and phase transformation of β-type Ti-35Nb-2Ta-3Zr alloy fabricated by 3D-Printing. J Alloys Compd 2019;790:117–26.

[3] Zhang L-C, Chen L-Y. A review on biomedical titanium alloys: recent progress and prospect. Adv Eng Mater 2019;21:1801215.

[4] Xie L, Wang L, Wang K, Yin G, Fu Y, Zhang D, et al. TEM characterization on microstructure of Ti–6Al–4V/Ag nanocomposite formed by friction stir processing. Materialia 2018;3:139–44.

[5] Wang L, Xie L, Zhang L-C, Chen L, Ding Z, Lv Y, et al. Microstructure evolution and superelasticity of layer-like NiTiNb porous metal prepared by eutectic reaction. Acta Mater 2018;143:214–26.

[6] Wang L, Xie L, Lv Y, Zhang L-C, Chen L, Meng Q, et al. Microstructure evolution and superelastic behavior in Ti-35Nb-2Ta-3Zr alloy processed by friction stir processing. Acta Mater 2017;131:499–510.

[7] Zhu Y, Tian X, Li J, Wang H. Microstructure evolution and layer bands of laser melting deposition Ti–6.5 Al–3.5 Mo–1.5 Zr–0.3 Si titanium alloy. J Alloys Compd 2014;616:468–74.

[8] Li YY, Ma SY, Liu CM, Zhang M. Microstructure and mechanical properties of Ti-6.5 Al-3.5 Mo-1.5 Zr-0.3 Si alloy fabricated by arc additive manufacturing with post heat treatment. Key Eng Mater Trans Tech Publ 2018:161–9.

[9] Filip R, Kubiak K, Ziaja W, Sieniawski J. The effect of microstructure on the mechanical properties of two-phase titanium alloys. J Mater Process Technol 2003;133:84–9.

[10] Huang L, Geng L, Li A, Wang G, Cui X. Effects of hot compression and heat treatment on the microstructure and tensile property of Ti–6.5 Al–3.5 Mo–1.5 Zr–0.3 Si alloy. Mater Sci Eng A 2008;489:330–6.

[11] Huang L, Geng L, Zheng P, Li A, Cui X. Hot tensile characterization of Ti–6.5 Al–3.5 Mo–1.5 Zr–0.3 Si alloy with an equiaxed microstructure. Mater Des 2009;30:838–41.

[12] Hanghang Y, Zekun Y, Jun G, Hongzhen G, Yingying L, Min W. Influence of gradient heat treatment on microstructure and microhardness in weld seam of Ti3Al/TC11 dual alloys. Rare Met Mater Eng 2010;39:22–6.

[13] Gu Y, Zeng F, Qi Y, Xia C, Xiong X. Tensile creep behavior of heat-treated TC11 titanium alloy at 450–550° C. Mater Sci Eng A 2013;575:74–85.

[14] Song H-W, Zhang S-H, Cheng M. Dynamic globularization kinetics during hot working of a two phase titanium alloy with a colony alpha microstructure. J Alloys Compd 2009;480:922–7.

[15] Jing L, Fu R, Wang Y, Qiu L, Yan B. Discontinuous yielding behavior and microstructure evolution during hot deformation of TC11 alloy. Mater Sci Eng A 2017;704:434–9.

[16] Xin L, Shiqiang L, Kelu W, Fu M, Zhenxi L, Chunxiao C. Hot deformation mechanism and process optimization for Ti-Alloy Ti-6.5 Al-3.5 Mo-1.5 Zr-0.3 Si during α+ β forging based on murty criterion. Rare Met Mater Eng 2008;37:577–83.

[17] Song H, Wang Z-J, He X-D, Duan J. Self-healing of damage inside metals triggered by electropulsing stimuli. Sci Rep 2017;7:7097.

[18] Lu Z, Guo C, Li P, Wang Z, Chang Y, Tang G, et al. Effect of electropulsing treatment on microstructure and mechanical properties of intermetallic Al3Ti alloy. J Alloys Compd 2017;708:834–43.

[19] Hosoi A, Nagahama T, Ju Y. Fatigue crack healing by a controlled high density electric current field. Mater Sci Eng A 2012;533:38–42.

[20] Hui S, Wang Z-J, Gao T-J. Effect of high density electropulsing treatment on formability of TC4 titanium alloy sheet. Trans Nonferrous Met Soc China 2007;17:87–92.

[21] Lou Y, Wu H. Improving machinability of titanium alloy by electro-pulsing treatment in ultra-precision machining. Int J Adv Manuf Technol 2017;93:2299–304.

[22] Loskutov S. Effect of electropulse treatment on the structure of the surface layer of alloy VT3-1. Met Sci Heat Treat 2006;48:261–3.

[23] Konovalov S, Komissarova I, Ivanov Y, Gromov V, Kosinov D. Structural and phase changes under electropulse treatment of fatigue-loaded titanium alloy VT1-0. J Mater Res Technol 2019;8:1300–7.

[24] González-Fernández L, Risueño E, Pérez-Sáez R, Tello M. Infrared normal spectral emissivity of Ti–6Al–4V alloy in the 500–1150 K temperature range. J Alloys Compd 2012;541:144–9.

[25] Conrad H, Karam N, Mannan S. Effect of electric current pulses on the recrystallization of copper. Scr Metall 1983;17:411–6.

[26] Conrad H. Effects of electric current on solid state phase transformations in metals. Mater Sci Eng A 2000;287:227–37.

[27] Conrad H. Electroplasticity in metals and ceramics. Mater Sci Eng A 2000;287:276–87.

[28] Conrad H. Thermally activated plastic flow of metals and ceramics with an electric field or current. Mater Sci Eng A 2002;322:100–7.

[29] Conrad H, Sprecher A, Cao W, Lu X. Electroplasticity—the effect of electricity on the mechanical properties of metals. JOM 1990;42:28–33.

[30] Conrad H, Karam N, Mannan S. Effect of prior cold work on the influence of electric current pulses on the recrystallization of copper. Scr Metall 1984;18:275–80.

[31] Ma B, Zhao Y, Bai H, Ma J, Zhang J, Xu X. Gradient distribution of mechanical properties in the high carbon steel induced by the detour effect of the pulse current. Mater Des 2013;49:168–72.

[32] Yu J, Zhang H, Deng D, Liu Q, Hao S. Analysis of the relationship of crack arrest effects with fusion zone size by current detour and Joule heating. Int J Adv Manuf Technol 2016;87:1465–74.

[33] Wei S, Wang G, Deng D, Rong Y. Microstructure characterization and thermal behavior around crack tip under electropulsing. Appl Phys A 2015;121:69–76.

[34] Yu T, Deng D, Wang G, Zhang H. Crack healing in SUS304 stainless steel by electropulsing treatment. J Clean Prod 2016;113:989–94.

[35] Ho J, Collings E. Anomalous electrical resistivity in titanium-molybdenum alloys. Phys Rev B 1972;6:3727.

[36] Ouchi C, Iizumi H, Mitao S. Effects of ultra-high purification and addition of interstitial elements on properties of pure titanium and titanium alloy. Mater Sci Eng A 1998;243:186–95.

[37] Ames SL, McQuillan A. The resistivity-temperature-concentration relationships in the system niobium-titanium. Acta Metall 1954;2:831–6.